

Dendrite-Free Li-Metal Anode Enabled by Dendritic Structure

Hongyu Zhang, Shunlong Ju, Guanglin Xia,* Dalin Sun, and Xuebin Yu*

The practical application of Li-metal anode in high-energy rechargeable Li batteries is still hindered by the uncontrollable formation of Li dendrites. Here, a facile way is reported to stabilize Li-metal anode by building dendrite-like Li_3Mg_7 alloys enriched with Li-containing polymers as the physical protecting layer and LiH as the Li-ion conductor. This unique dendritic structure effectively reduces local current density and accommodates volume change during the repeated Li plating/stripping process. More importantly, lithiophilic Li_3Mg_7 alloys not only guide the uniform Li deposition down into the below Li metal upon Li deposition, but also thermodynamically promote the extraction of Li during the reverse Li stripping process, which suppresses the parasitic reactions occurring on the surface of Li metal and hence inhibits the formation of Li dendrites. Moreover, the facile diffusion of Mg from Li_3Mg_7 alloys toward Li metal below is thermodynamically permitted, which leads to a uniform distribution of LiMg alloys inside the whole electrode and thus benefits long-term deep cycling stability. As a result, the protected Li-metal anode delivers stable and dendrite-free cycling performance at 10 mA h cm^{-2} for over 900 h. When coupling this anode with LiFePO_4 and S cathodes, the thus-assembled full cells exhibit superior cycling stability.

of Li dendrites and the large volume change during Li plating/stripping process could induce repeated cracking and the regeneration of brittle SEI, which accelerates the uncontrollable growth of dendritic or mossy Li and the isolation of Li dendrites to form “dead Li.”^[5,6] These inherent issues lead to short lifespan and could cause failure and even short-circuit with fire.^[7,8]

To tackle these issues, considerable efforts have been proposed to inhibit the growth of Li dendrites and enhance the cycling stability of Li-metal anodes (LMAs), including the modification of SEI and building 3D host or alloy anodes.^[9,10] Since SEI plays an important role in stabilizing the surface of Li metal, building robust artificial SEI layers, including polymers, inorganic salts with high ionic conductivity, and lithiophilic metallic alloys, is proved to be an effective way in suppressing the formation of Li dendrites. Among them, flexible polymers could mechanically inhibit the growth of Li


1. Introduction

Commercial Li-ion batteries with graphite anodes are gradually reaching their theoretical specific capacity limit of $\approx 372 \text{ mA h g}^{-1}$ in the past 30 years. To satisfy the ever-increasing demands of electric vehicles, the fabrication of electrochemical energy storage system with higher energy and power density is of great importance.^[1] Among all anode candidates, metallic Li, due to its ultrahigh theoretical capacity of 3860 mA h g^{-1} and its lowest electrochemical potential (-3.04 V vs standard hydrogen electrode), has been regarded as the “holy Grail” of electrode.^[2,3] Li, however, is prone to react with liquid electrolyte to form nonuniform and brittle solid electrolyte interface (SEI) accompanied by the excessive consumption of both lithium and electrolyte,^[3,4] which results in sustained capacity fading and low Coulombic efficiency. More importantly, the continuous growth

dendrites and prevent the penetration of Li dendrites to some extent, while inorganic salts with high Li ion conductivity could further homogenize the Li-ion flux during Li plating process, leading to the suppressed formation of Li dendrites. Besides, due to the important role of the initial nucleation behavior in determining the growth of plated Li, it has been widely demonstrated that the decoration of lithiophilic metals or their alloys on Li metal (Ag,^[11] Al,^[12] Sn,^[13] and Mg^[14]) could effectively guide the uniform nucleation and deposition of Li via reducing Li nucleation barrier. Nevertheless, the inevitable volume change involved during repeated Li stripping/plating process is still capable of breaking fragile SEI layers, thus resulting in continuous reaction between Li metal with electrolytes. Therefore, in order to minimize this detrimental effect, 3D conductive hosts, e.g., metallic foam,^[15] MXene aerogel,^[16] and nanostructured carbon frameworks,^[17,18] have been adopted to accommodate the huge volume expansion of Li. Moreover, based on Chazalviel's theory, designing conductive hosts with high surface area could also lower the local current density and thus effectively alleviate the growth of Li dendrites. Unfortunately, the introduction of a large amount of inactive weight of hosts would tremendously decrease the energy density of LMAs for practical applications.

Inspired from the role of lithiophilic alloys in guiding uniform Li deposition and 3D hosts in accommodating the volume

H. Y. Zhang, S. L. Ju, Dr. G. L. Xia, Prof. D. L. Sun, Prof. X. B. Yu
Department of Materials Science
Fudan University
Shanghai 200433, China
E-mail: xianguanglin@fudan.edu.cn; yuxuebin@fudan.edu.cn

 The ORCID identification number(s) for the author(s) of this article can be found under <https://doi.org/10.1002/adfm.202009712>.

DOI: 10.1002/adfm.202009712

change of Li, building conductive lithiophilic alloys with well-designed 3D structures on the surface of Li metal may be an ideal approach to develop stable LMAs with high energy density. Herein, we report a facile way to fabricate dendrite-like Li_3Mg_7 alloys enriched with polymers, serving as the physical protecting layer, and LiH, serving as the Li-ion conductor, on the surface of Li metal (denoted as $\text{Li}_3\text{Mg}_7@\text{Li}$), based on in situ electroless reaction between Li metal and dibutylmagnesium (MgBu_2). During the reaction between MgBu_2 and Li metal, MgBu_2 could be facilely reduced by Li metal toward the formation of both lithiophilic Li_3Mg_7 alloys and LiBu and subsequently, the thus-formed LiBu could be in situ decomposed into Li-containing polymers and LiH. First, the porous structure constructed by dendrite-like Li_3Mg_7 alloys exhibits the feature of 3D current collector, which could not only reduce the local current density and hence delay the formation of Li dendrites, but also accommodate large volume change of the electrode during repeated Li plating and stripping, leading to favorable cycling stability. More importantly, both theoretical calculation and experimental observation demonstrate that Li_3Mg_7 alloys could not only guide the uniform Li deposition down into the below Li metal upon Li plating, but also thermodynamically promote the extraction of Li from the thus-formed LiMg alloys (LiMg alloys in this work represent various Li_xMg_y alloys in situ formed upon Li plating/stripping process) during the reverse Li stripping process, which could hence avoid the parasitic reactions occurring on the surface of Li metal and result in the formation of stable electrode/electrolyte interface for inhibiting the generation of Li dendrites. Interestingly, it is

thermodynamically favorable for the facile diffusion of Mg from Li_3Mg_7 alloys toward Li metal below, which facilitates the uniform distribution of LiMg alloys inside the whole electrode and hence results in excellent long-term deep cycling stability. As a result, the as-obtained $\text{Li}_3\text{Mg}_7@\text{Li}$ anode exhibits a long life up to 2200 h with an overpotential of ≈ 8 mV at 0.5 mA cm^{-2} and superior deep stripping/plating capacities up to 10 mA h cm^{-2} for over 900 h. More impressively, the full cell using the sulfur as cathode and the protected Li metal as anode exhibits an ultrahigh reversible capacity of 640 mA h g^{-1} after 500 cycles at a high current density of 2 C .

2. Results and Discussion

Since MgBu_2 exhibits a unique chain structure that has one Mg atom bonded with two *n*-butyls and good solubility in heptane, it could be homogeneously distributed on the surface of Li foils toward uniform modification of Li-metal anode. Therefore, as illustrated in **Figure 1A**, dendritic Li_3Mg_7 alloys enriched with Li-containing polymer and LiH decorated on Li foils ($\text{Li}_3\text{Mg}_7@\text{Li}$) were fabricated through in situ electroless reduction of MgBu_2 with Li foils (i.e., $7\text{MgBu}_2 + 17\text{Li} \rightarrow \text{Li}_3\text{Mg}_7 + 14\text{LiBu}$), which results in the formation of Li_3Mg_7 alloys and LiBu, followed by the fast decomposition of thus-formed liquid LiBu into LiH and Li-containing polymers (i.e., $\text{LiBu} \rightarrow \text{LiH} + \text{Li-containing polymers}$). After the in situ reaction at 200°C , X-ray diffraction (XRD) pattern (**Figure 1B**) confirms the formation of Li_3Mg_7 while Fourier-transform

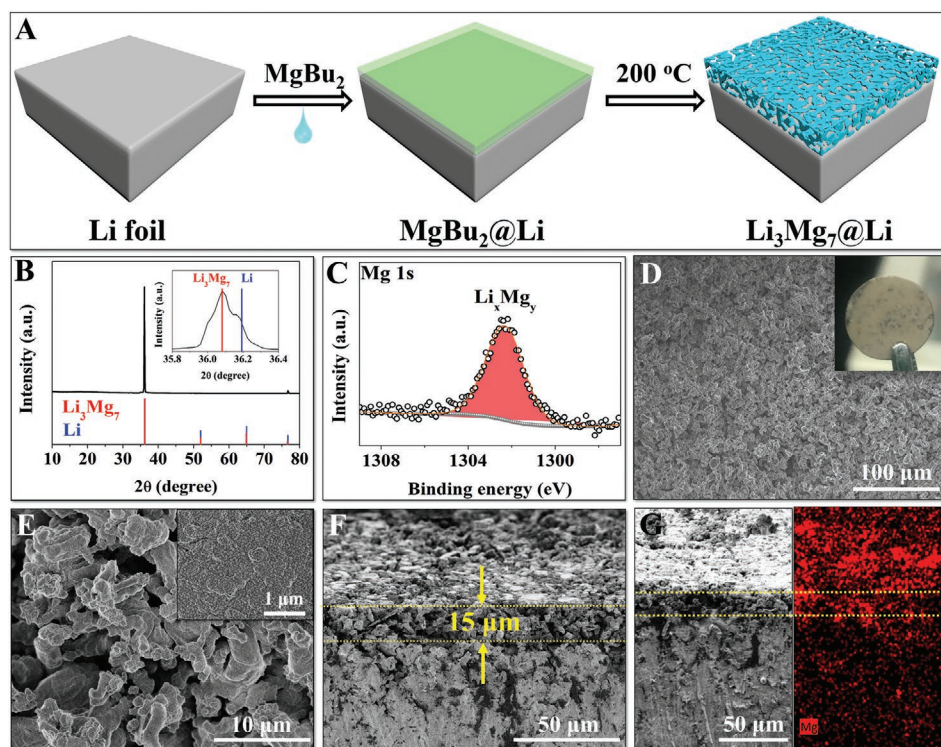


Figure 1. A) Schematic illustration of the synthesis of $\text{Li}_3\text{Mg}_7@\text{Li}$ electrode. B) XRD pattern, C) high-resolution XPS spectra, and D) low-magnification (inset: the optical photograph of the as-obtained $\text{Li}_3\text{Mg}_7@\text{Li}$ anode), E,F) high-magnification, and G) cross-sectional SEM images of $\text{Li}_3\text{Mg}_7@\text{Li}$ electrode.

infrared spectroscopy (FTIR) spectra demonstrate the presence of LiH and Li-containing polymers (Figure S1, Supporting Information), which agrees well with the observation of Li_3Mg_7 alloys at 1302.4 eV, LiH at 55.5 eV, and Li-containing polymers at 282.5 and 284.8 eV indexed to Li–C and C–H bonds, respectively, in the X-ray photoelectron spectroscopy (XPS) spectra (Figure 1C and Figure S2, Supporting Information). In comparison with the flat surface of fresh Li metal (Figure S3A, Supporting Information), scanning electron microscopy (SEM) images (Figure 1D–G) illustrate that a uniform layer composed of dendritic Li_3Mg_7 alloys with a thickness of $\approx 15 \mu\text{m}$ was successfully fabricated on the surface of Li foil. To elucidate the mechanism for the formation of dendritic structure, the initial surface morphology of Li metal was studied after the electroless reaction at 80 °C before the decomposition of LiBu (Figure S4, Supporting Information). After the removal of unreacted LiBu and residual MgBu_2 , a dense layer of Li_3Mg_7 alloys with a thickness of only $\approx 2 \mu\text{m}$ was fabricated on the surface of Li metal (Figure S5, Supporting Information). In addition, the individual decomposition of LiBu on the surface of Li metals (denoted as LiH@Li) also results in the formation of a relatively flat surface, composed of LiH and Li-containing polymers (Figure S6, Supporting Information). Therefore, the formation of dendritic structure could be attributed to the fast and massive release of butene and butane resulting from the decomposition of liquid LiBu, serving as the liquid template to guide the synthesis of Li_3Mg_7 alloys, which finally transforms into LiH and Li-containing polymers on their surfaces. The large surface area and massive void space inside dendritic Li_3Mg_7 alloys could not only effectively reduce local current density to postpone the formation of Li dendrites, but also accommodate the volume change during repeated Li plating/stripping process as the role of 3D conductive hosts. The elemental mapping of Li_3Mg_7 @Li (Figure S7, Supporting Information) from top-view and cross-sectional view demonstrated the uniform distribution of Mg and C element on the surface of Li foil, which confirms the homogeneous distribution of Li_3Mg_7 alloys and Li-containing polymers. By comparison, upon decreasing the reaction temperature between Li foil and MgBu_2 down to 170 °C, although the dendritic Li_3Mg_7 alloys could still be formed, they were unevenly distributed on the surface of Li foil with partial regions of the surface being uncovered (Figure S8, Supporting Information), which could be attributed to slow reaction kinetics induced by the decrease of reaction temperature. On the other hand, upon increasing the temperature to 230 °C (Figure S9, Supporting Information), compact Li_3Mg_7 alloys chunks with flat surface and a thickness of around 20 μm , instead of dendritic structure (Figure S10, Supporting Information), could be observed on the surface of Li foils resulting from the melting of Li foils.

In order to investigate the role of Li_3Mg_7 alloys in suppressing the formation of Li dendrites, the nucleation overpotentials of Li plating, which is a key indicator for estimating the lithiophilic degree of the electrode, were first investigated (Figure S11, Supporting Information). A sharp drop in voltage to 27 mV, defined as the tip potential, could be initially observed upon Li plating on bare Li metal at 1 mA cm^{-2} , which could be attributed to the nucleation of Li metal. Subsequently, the voltage platform slowly increases to a relatively steady pla-

teau at 20 mV, which represents the mass-transfer-regulated overpotential. Therefore, the nucleation overpotential of bare Li-metal anode is calculated to be 7 mV according to the difference between the tip potential and the later stable voltage, indicating the presence of large nucleation barrier for Li deposition. Interestingly, no nucleation overpotential could be observed under the modification of Li_3Mg_7 alloys prepared under various conditions. These results demonstrate that Li_3Mg_7 alloys could serve as a solid solution to eliminate the nucleation overpotential of Li plating, which could homogenize the nucleation of Li metal and suppress the formation of Li dendrites.

Theoretical simulations based on density functional theory (DFT) calculations were further performed to understand the lithiophilicity of Li_3Mg_7 alloys. Under the most stable adsorption configuration, the binding energy between the Li_3Mg_7 (001) surface and Li could reach -1.94 eV , while this value is only -1.44 eV for Li metal (Figure 2A and Figure S12A, Supporting Information). More interestingly, upon the further lithiation of Li_3Mg_7 to form Li-rich alloys, e.g., Li_3Mg ,^[19] the binding energy of Li on Li_3Mg (001) surface could still achieve -1.78 eV (Figure 2C), which demonstrates that lithiophilic LiMg alloys provide favorable Li nucleation sites and hence effectively regulate Li plating process. Bader analysis confirms that a Li atom could donate $\approx 0.82|e|$ and $0.79|e|$ on Li_3Mg_7 (001) and Li_3Mg (001) surface, respectively, as visualized in the charge density difference plots (Figure 2B,D). By comparison, a Li atom accepts about $1.62|e|$ from metallic Li (Figure S12B, Supporting Information). This result validates that the presence of Mg enhances the delocalization of electrons on the deposited lithium, which contributes to the formation of metallic bonds between deposited Li and LiMg alloys. Therefore, Li atoms prefer to deposit on LiMg alloys rather than on metallic Li that has been plated already. Besides, the diffusion behavior of Li on the surface of LiMg alloys, which plays a significant role in tuning uniform Li electrodeposition, was further investigated. As shown in Figure 3E–H, the barriers for Li diffusion on the surface of Li_3Mg_7 (001) and Li_3Mg (001) were calculated to be 0.27 and 0.17 eV, respectively, while this value is only 0.045 eV for Li (001) surface (Figure S12C,D, Supporting Information), indicating the much lower tendency for the aggregation of Li atoms to form dendrites on the surface of LiMg alloys.^[20] In addition, it is interesting to note that the binding energy between LiH (001) surface and Li atom reaches -0.75 eV , much larger than that of bare Li (Figure S13A, Supporting Information), illustrating the lithiophobic nature of LiH. Meanwhile, a diffusion barrier as low as 0.040 eV could be obtained on LiH (001) surface (Figure S13B,C Supporting Information), which is even lower than that of bare Li. It verifies that the presence of LiH on the surface of dendritic Li_3Mg_7 alloys could induce fast diffusion of Li atoms on its surface toward the favorable deposition into Li_3Mg_7 alloys, leading to the suppressed formation of Li dendrites.

The electrochemical Li plating/stripping behavior of Li_3Mg_7 @Li anodes, in comparison with pristine Li metals, was subsequently conducted to evaluate the role of dendritic Li_3Mg_7 alloys enriched with LiH and Li-containing polymers in stabilizing LMAs. The presence of numerous defects and protuberance on the surface of bare Li (Figure S3A, Supporting Information) causes “island deposition” of Li,^[21] and hence results in the formation of high-surface-area dendritic Li during Li plating

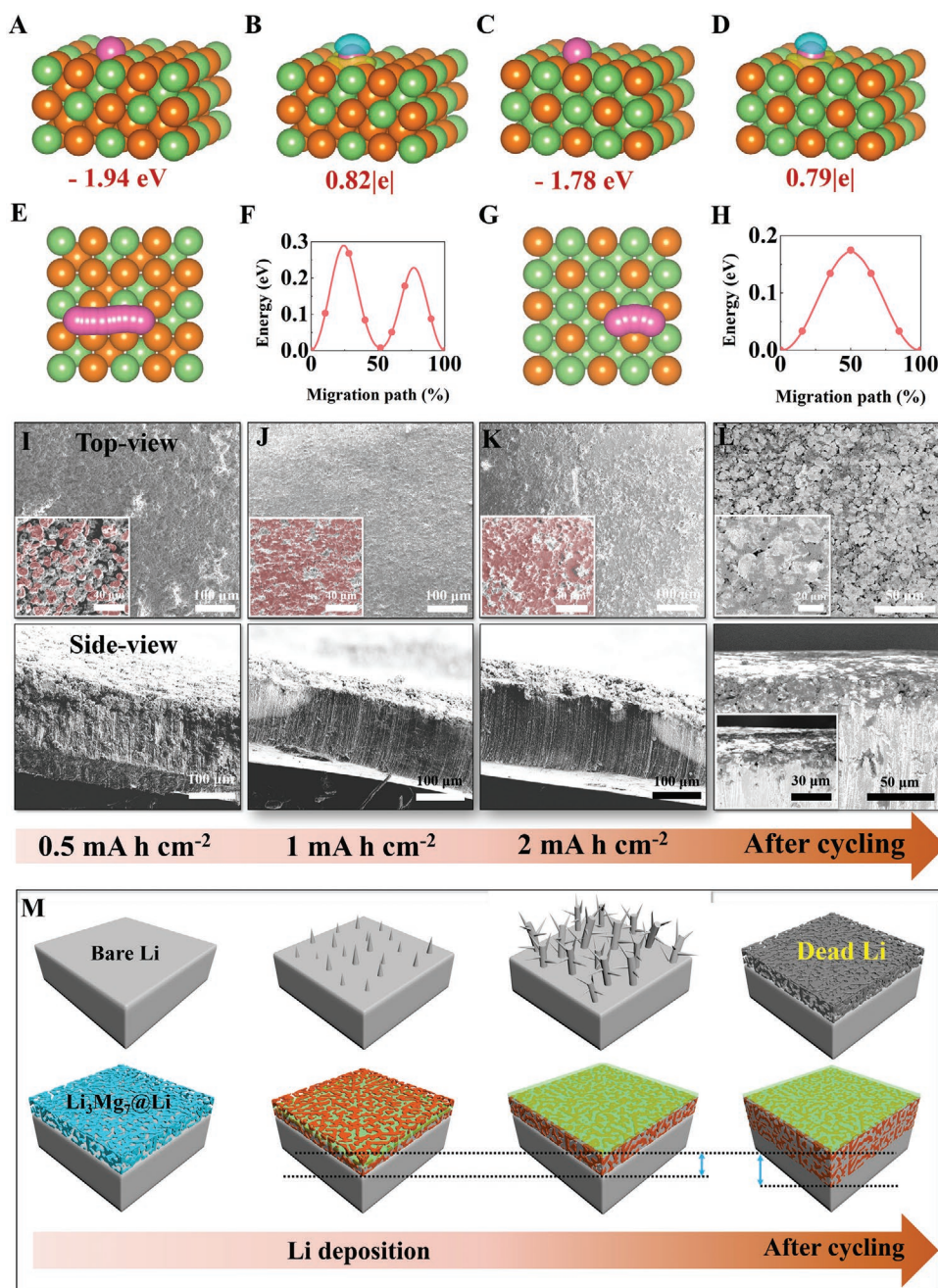


Figure 2. A,C) The adsorption configuration and B,D) charge density difference plot of Li on A,B) Li_3Mg_7 (001) surface and C,D) Li_3Mg (001) surface, respectively. Areas of charge accumulation are shown in yellow while depletion is shown in blue. E,G) The diffusion pathway and F,H) calculated energy profile of Li along diffusion path on E,F) Li_3Mg_7 (001) surface and G,H) Li_3Mg (001) surface, respectively. The orange, green, and pink balls denote Mg, Li, and adsorbed Li atoms, respectively. I–L) Top/side-view SEM images of $\text{Li}_3\text{Mg}_7@Li$ anode deposited with 0.5 , 1 , 2 mA h cm^{-2} of Li at 1 mA cm^{-2} and after 150 cycles of Li stripping/plating at 1 mA cm^{-2} , 1 mA h cm^{-2} , 1 mA h cm^{-2} , respectively. Insets are magnified images of the corresponding SEM images. M) Schematic illustration of Li deposition behavior on bare Li and $\text{Li}_3\text{Mg}_7@Li$, respectively, upon Li deposition.

(Figure S3B, Supporting Information). The growth of dendritic Li and the uneven deposition of Li became increasingly serious with the increase of Li deposition capacity from 1 to 2 mA h cm^{-2} (Figure S3C,D, Supporting Information) and clear “dead Li” with a thickness of over $80 \mu\text{m}$ could be observed after only 100 cycles (Figure S3E, Supporting Information). As a result, the overvoltage of Li//Li cell sharply increased to 100 mV after

only 400 h at 1 mA cm^{-2} with a fixed capacity of 1.0 mA h cm^{-2} (Figure S14, Supporting Information). It could eventually lead to the irreversible depletion of Li and electrolyte and even the pierce of separator. By comparison, the $\text{Li}_3\text{Mg}_7@Li$ electrode could stably cycle without obvious increase of overvoltage under identical condition, exhibiting a voltage hysteresis of less than 11 mV after 1300 h , which indicates that the decoration of

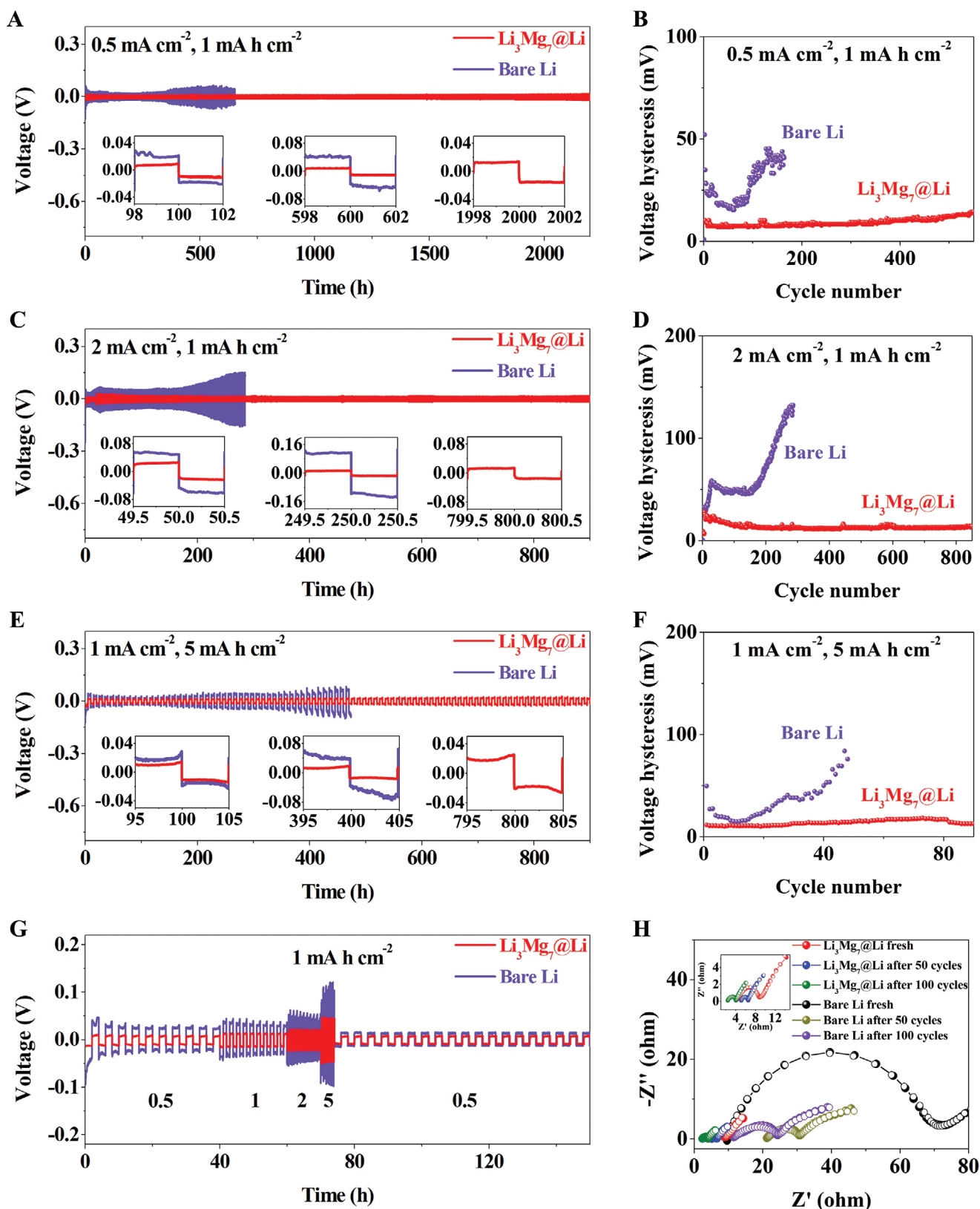


Figure 3. A,C,E) Galvanostatic discharge/charge voltage profiles and B,D,F) average voltage hysteresis of $\text{Li}_3\text{Mg}_7@\text{Li}$ and bare Li in symmetric cells at various current densities with different areal capacities, respectively. G) Rate performance comparison of $\text{Li}_3\text{Mg}_7@\text{Li}$ and bare Li in symmetric cells at various current densities. H) EIS of $\text{Li}_3\text{Mg}_7@\text{Li}$ electrode and bare Li electrode in symmetric cells before and after cycling at 1 mA cm^{-2} .

lithiophilic Li_3Mg_7 alloys enriched with LiH and Li-containing polymers could guide uniform Li deposition and suppress the growth of Li dendrites. Interestingly, owing to the modification of Li_3Mg_7 alloys enriched with LiH and Li-containing polymers, the thus-formed $\text{Li}_3\text{Mg}_7@\text{Li}$ electrodes fabricated at both 170 and 230 °C exhibit a superior cycling stability compared with bare Li metal. A clear increase of overpotential to 55 mV, however, could be observed for $\text{Li}_3\text{Mg}_7@\text{Li}$ electrode fabricated at 170 °C after 600 h and $\text{Li}_3\text{Mg}_7@\text{Li}$ electrode fabricated at 230 °C after 800 h, respectively. This result indicates that the well-designed dendrite-like structure, which could lower the local current density, regulate the electrical field distribution, and alleviate the volume change of Li metal, plays an important role in stabilizing the stripping/plating performance of Li metals. Moreover, even without the presence of Li_3Mg_7 alloys, the as-fabricated LiH@Li anode could still maintain a stable voltage profile for over 400 h, suggesting that the protection of the Li-containing polymers and LiH with high Li-ion conductivity could also alleviate the side reaction between Li and electrolyte and suppress the formation of Li dendrites and dead Li (Figure S15, Supporting Information). Therefore, the superior cycling performance of $\text{Li}_3\text{Mg}_7@\text{Li}$ anode could be attributed to the synergistic effect of dendritic Li_3Mg_7 alloys, which could guide the uniform Li deposition, and the protective role of Li-containing polymers and LiH, leading to the suppressed formation of Li dendrites.

In order to elucidate the detailed plating behavior of Li foils decorated with dendritic Li_3Mg_7 alloys, SEM measurement was conducted to investigate their morphologic change upon Li deposition. After the modification with dendritic Li_3Mg_7 alloys, Li prefers to grow inside the void space of dendritic Li_3Mg_7 alloys in the shape of nodule (Figure 2I) without the observation of any Li dendrites upon increasing the Li plating capacity from 0.5 to 1 mA h cm⁻² (Figure 2J). When increasing the plating level to 2 mA h cm⁻², the inside space of dendritic Li_3Mg_7 alloys could be largely occupied by densely deposited Li (Figure 2K), exhibiting a smooth and flat surface, which could effectively reduce the side reaction and possibility of short circuit. Impressively, upon the reverse extracting 0.5, 1, 2 mA h cm⁻² of Li from $\text{Li}_3\text{Mg}_7@\text{Li}$ anode, the dendritic structure of Li_3Mg_7 alloys could be fully recovered, indicating stable structural integrity of $\text{Li}_3\text{Mg}_7@\text{Li}$, which enhances the stable reversibility of Li stripping/plating process (Figure S16, Supporting Information). Accordingly, a nodule-like, dendrite-free, and dense deposition without any distinguished cracks could still be observed with a thickness of around 20 μm even after 150 cycles of Li stripping/plating process (Figure 2L), which is similar to its original thickness. By comparison, although the formation of Li dendrites could also be suppressed after 150 cycles for $\text{Li}_3\text{Mg}_7@\text{Li}$ anode prepared at both 170 and 230 °C (Figures S17 and S18, Supporting Information), corresponding well with their superior cycling stability compared with pure Li metal, Li is plated in the form of separated chunks with obvious cracks on their surfaces. This result demonstrates that the inhomogeneous distribution of dendrite-like Li_3Mg_7 alloys prepared at 170 °C and the formation of dense Li_3Mg_7 alloys with flat surface in the $\text{Li}_3\text{Mg}_7@\text{Li}$ electrode prepared at 230 °C could weaken their capability of guiding uniform and dense deposition of Li and releasing stress induced by volume change during repeated

Li stripping/plating process. Consequently, this result verifies that lithiophilic Li_3Mg_7 alloys with dendritic structure could not only guide the uniform and compact deposition of Li, but also effectively accommodate the volume change of Li, which, coupled with the protective role of Li-containing polymers and LiH that could simultaneously regulate uniform Li-ion flux,^[6,22] could effectively inhibit the growth of dendritic Li and avoid the formation of “dead Li.” As a result, when symmetric cells were cycled at 0.5 mA cm⁻² for 1 mA h cm⁻², $\text{Li}_3\text{Mg}_7@\text{Li}$ electrode shows low overpotential (≈8 mV) with negligible voltage fluctuation and ultralong lifespan of over 2200 h in ether-based electrolyte (Figure 3A,B), while a clear increase of overpotential was observed for bare Li metal after only 60 cycles. Moreover, when the current density is increased to 2 and 3 mA cm⁻² (Figure 3C,D and Figure S19C,D, Supporting Information), the voltage hysteresis of $\text{Li}_3\text{Mg}_7@\text{Li}$ anode confirms superior stability with a negligible voltage fluctuation during cycling stripping/plating process. Particularly, the overpotential of bare Li metal was increased to 60 mV after only 30 cycles at 2 mA cm⁻². In contrast, after cycling for over 800 h, $\text{Li}_3\text{Mg}_7@\text{Li}$ anode could still operate with only slight change in overpotential. Upon further increasing the current density to 10 mA cm⁻² with an areal capacity of 10 mA h cm⁻² (Figure S20, Supporting Information), the overpotential of bare Li increases drastically after only 40 h of cycling. Under the protection of Li_3Mg_7 with flat surface, although the lifespan of $\text{Li}_3\text{Mg}_7@\text{Li}$ electrode fabricated at 230 °C is prolonged to some extent, a rapid increase of overpotential could be observed after 220 h. In strong contrast, $\text{Li}_3\text{Mg}_7@\text{Li}$ with dendrite-like surface exhibits a long cycling life of over 500 h with a low voltage hysteresis of 45 mV under identical condition.

Interestingly, upon the proceeding of the cycling process, a clear diffusion of elemental Mg downward to the bottom of Li foils could be observed by the cross-sectional elemental mapping results (Figure S21, Supporting Information) and this trend becomes more obvious after prolonging to 300 cycles (Figure S22, Supporting Information). It reveals that Mg in Li-poor LiMg alloy (i.e., Li_3Mg_7) could diffuse to its backside to generate Li-rich LiMg alloy upon cycling. DFT calculation demonstrates that, under the stable configuration of both $\text{Li}_3\text{Mg}_7/\text{Li}$ and $\text{Li}_3\text{Mg}/\text{Li}$ system, the diffusion of Mg into Li metal results in a significant decrease in the systematic energy, indicating that the diffusion of Mg is thermodynamically spontaneous from LiMg alloys with both high and low lithium concentrations into Li metal (Figure 4A,B). As expected, the energy difference of $\text{Li}_3\text{Mg}_7/\text{Li}$ system is much larger than that of $\text{Li}_3\text{Mg}/\text{Li}$, suggesting that the diffusion driving force is stronger in LiMg alloys that have high Mg concentration. These results directly validate the favorable diffusion of Mg downward into Li metals toward the formation of uniform Li-rich LiMg alloys based on the molecular level, which could uniformly strengthen the interaction between the upper LiMg alloys and the bottom Li foils and hence effectively preserve the structural integrity of the whole electrode, leading to improved cycling stability. Subsequently, the reverse Li stripping process was further simulated using the $\text{Li}_3\text{Mg}/\text{Li}$ interface model, owing to the formation of Li-rich LiMg alloys on the surface upon Li plating and the diffusion of Mg downward. The diffusion of Li vacancy (V_{Li}) upon removing one Li atom from the surface

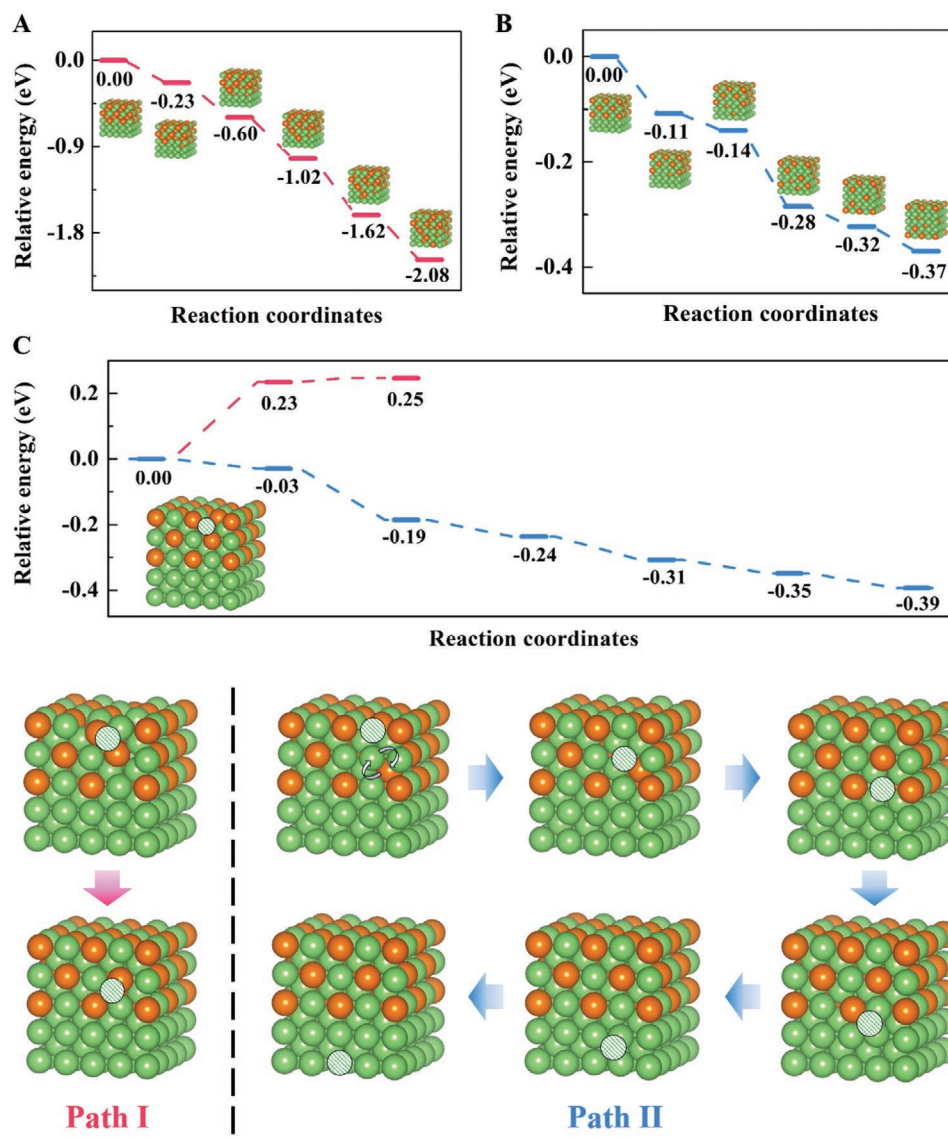


Figure 4. Relative energy diagram for Mg diffusion along the interfaces in A) Li₃Mg₇/Li and B) Li₃Mg/Li system and C) Li vacancy diffusion along the thus-formed Li₃Mg/Li interface upon Li plating.

of Li₃Mg to simulate Li stripping process is calculated in two potential diffusion modes, i.e., path I (red lines) representing the diffusion of the V_{Li} via exchanging with adjacent Li atoms, and path II (blue lines) representing the diffusion of V_{Li} via the assistance of Mg atoms (Figure 4C). Interestingly, the corresponding energy curves demonstrate that the diffusion of V_{Li} is thermodynamically favorable under the assistance of Mg atoms in the thus-formed LiMg alloys. It validates that the alloying of Li with Mg could not only guide the uniform Li deposition into the below Li metal, but also effectively promote the extraction of Li from thus-formed LiMg alloys during the reverse Li stripping process. Accordingly, the parasitic reactions occurring on the surface of Li metal during repeated stripping/plating process could be largely avoided, leading to the formation of stable electrode/electrolyte interface for inhibiting the formation of Li dendrites.

More importantly, the favorable diffusion of Mg into Li metals could realize the uniform distribution of LiMg alloys inside the whole electrode and thus effectively enhance its capability of regulating uniform Li deposition upon long-term deep Li stripping/plating process. Therefore, upon increasing the stripping/plating capacity to as high as 5 and 10 mA h cm⁻², the symmetric Li₃Mg₇@Li cells function well for over 900 h under a fixed capacity as high as 5 mA h cm⁻² (Figure 3E,F) and 10 mA h cm⁻² (Figure S23, Supporting Information) at 1 mA cm⁻² with low overpotential. When increasing Li plating capacity to 5 and 10 mA h cm⁻², not only the formation of Li dendrites could be completely inhibited, but also Li prefers to grow in the shape of thick nodule rather than the common Li dendrites densely distributed on the surface of LiMg alloys even after the space of porous structure of Li₃Mg₇ alloys is fully filled, which provides direct evidence to the important role of

dendritic LiMg alloys in guiding and homogenizing the deposition of Li, leading to dendrite-free Li plating/stripping process. After the deposition of Li of 5 and 10 mA h cm⁻², the thickness of plated Li layers is only 31 and 57 μm (Figure S24, Supporting Information), respectively, while these values are significantly increased to 86 and 116 μm (Figure S25, Supporting Information), respectively, for pristine Li metal due to serious formation of porous Li dendrites with uneven distribution. In term of the counter electrode of the symmetric cell, when 10 mA h cm⁻² of Li was stripped (Figure S26, Supporting Information), fluctuant surface with large pits was abundantly formed on bare Li, demonstrating the uneven stripping of Li. Under the protection of Li₃Mg₇ with flat surface, the Li₃Mg₇@Li electrode prepared at 230 °C shows a more uniform surface. However, a few holes and cracks could also be observed on the surface with the exposure of some fresh Li underneath, which results from large volume change induced by Li stripping process. By comparison, the dendritic structure of Li₃Mg₇@Li prepared at 200 °C could be well preserved even after stripping 10 mA h cm⁻² of Li, which directly demonstrates that the stress induced by the large volume change during Li stripping could be effectively alleviated by the dendritic Li₃Mg₇ alloys uniformly distributed on Li metal anode. Moreover, the symmetric cells are also tested in carbonate-based electrolyte, in which Li₃Mg₇@Li electrode shows stable cycling for 1000 and 500 h with low overpotential of 50 and 100 mV at 1 mA cm⁻² (Figure S27, Supporting Information) and 2 mA cm⁻² (Figure S28, Supporting Information), respectively. These results indicate that dendritic Li₃Mg₇ alloys enriched with LiH and Li-containing polymers effectively guide uniform and dense deposition of Li and meanwhile, the diffusion of Mg downward to form Li-rich LiMg alloy effectively preserves structural integrity of the whole electrode and promote the lithiation and delithiation of LiMg alloys toward stable stripping and plating process, leading to excellent cycling stability.

To intuitively investigate morphology evolution of bare Li and Li₃Mg₇@Li, in situ optical microscopy observation was conducted. Uneven moss-like dendrites grow quickly on the surface of bare Li at 5 mA cm⁻² after 10 min, and the thickness of the electrode increases severely owing to the rapid growth of porous Li dendrites after 30 min (Figure S29, Supporting Information). In strong contrast, Li₃Mg₇@Li electrode exhibits smooth and dense deposition of Li, coinciding well with SEM results. Even at a high current density of 10 mA cm⁻² (Figure 5A,B), Li₃Mg₇@Li electrode presents uniform and compact plating of Li after 20 min, while rigorous growth of Li dendrites was observed for bare Li metal. This observation provides direct evidence to the capability of dendritic Li₃Mg₇ alloys enriched with Li-containing polymer and LiH in stabilizing the interfaces of LMAs and inhibiting the growth of Li dendrites. In addition, the Li₃Mg₇@Li anode exhibits a superior rate capability than bare Li metal (Figure 3G). Stable cycling performance with a small voltage hysteresis value of 8, 12, 20, and 40 mV was obtained for Li₃Mg₇@Li at 0.5, 1, 2, and 5 mA cm⁻², respectively, which is much lower than those of bare Li metal, indicating the enhanced stripping and plating kinetics for Li₃Mg₇@Li anode. The voltage hysteresis turns back to 7 mV after the current density drops to 0.5 mA cm⁻², demonstrating the excellent reversible stripping/plating process of Li₃Mg₇@Li. Electrochemical impedance spectra (EIS) analysis (Figure S30,

Supporting Information) verifies that, due to the uniform and dense deposition of Li induced by dendritic Li₃Mg₇ alloys, both the interfacial charge transfer resistance (R_{ct}) and the SEI resistance (R_{SEI}) were obviously lower than that of bare Li metal (Figure 3H and Table S1, Supporting Information). It demonstrates that dendritic Li₃Mg₇ alloys endow Li-metal anode with fast kinetic of Li stripping/plating process and stable SEI layers, which not only facilitates the uniform Li deposition and prevents the formation of Li dendrites, but also reduces the polarization of continuous Li plating/stripping process. It is worth to note that a much lower value of R_{ct} and R_{SEI} for LiH@Li anode than that of bare Li before and after cycling (Figure S31, Supporting Information), indicating the fast charge transfer in the protective layers composed of Li-containing polymers and LiH. In addition, the exchange current density (I_0) for Li plating/stripping of LiH@Li (2.13 mA cm⁻²) is also much higher than that of bare Li (0.41 mA cm⁻²), indicating the fast Li ion transfer on electrode/electrolyte interface due to the low surface diffusion barrier of LiH (Figure S13B,C, Supporting Information). Induced by the synergistic effect of dendritic Li₃Mg₇ alloys and the protective layers composed of Li-containing polymer and LiH, the I_0 for Li plating/stripping of Li₃Mg₇@Li electrode could be further enhanced to 3.71 mA cm⁻² (Figure S32, Supporting Information).

In-depth XPS via Ar ion etching was further adopted to detect the evolution of chemical composition of Li₃Mg₇@Li electrode. After 20 cycles of Li stripping/plating process (Figure 5C and Figure S33, Supporting Information), characteristic peaks of LiMg alloys, LiH, and Li-containing polymers are well preserved, which provides additional evidence to the excellent stability of Li₃Mg₇@Li anode. Two peaks of 399.9 and 398.1 eV in the N 1s spectrum are related to the formation of LiN_xO_y and Li₃N on the surface of Li₃Mg₇@Li electrode due to the decomposition of LiTFSI and LiNO₃ in ether-based electrolyte, which corresponds well with the peak at around 54.9 eV in the Li 1s spectrum. In parallel, the peak at 684.8 eV in the F 1s spectrum and the peak at 56.0 eV in the Li 1s spectrum illustrate the formation of LiF owing to the break of C–F bonds in LiTFSI. Upon the increase of etching time, the signals of LiN_xO_y and LiF, which are typical components of SEI layers, decrease significantly with the appearance of metallic Li (Li⁰), while only slight decrease of signals of LiN_xO_y and LiF could be observed for bare Li metal with the complete absence of metallic Li (Figure S34, Supporting Information). It demonstrates that the modification of dendritic Li₃Mg₇ alloys could effectively stabilize the formation of SEI layers and promote the uniform and dense deposition of Li metal. More interestingly, upon the proceeding of cycling process, the characteristic peak of Li_xMg_y alloys in the Mg 1s spectrum gradually moves to a lower binding energy owing to the increase of Li content in the as-formed Li_xMg_y alloys resulting from the diffusion of Mg downward to Li metals. Meanwhile, the signal of Li-rich LiMg alloy appears after etching of 300 nm in depth in the Mg 1s spectrum, whereas the presence of Li-rich LiMg alloy in the fresh Li₃Mg₇@Li electrode could be clearly detected after etching of only 150 nm in depth (Figure S35, Supporting Information). These results confirm the facile diffusion of Mg downward to Li metals upon cycling Li stripping/plating process, which is consistent with the energy-dispersive X-ray

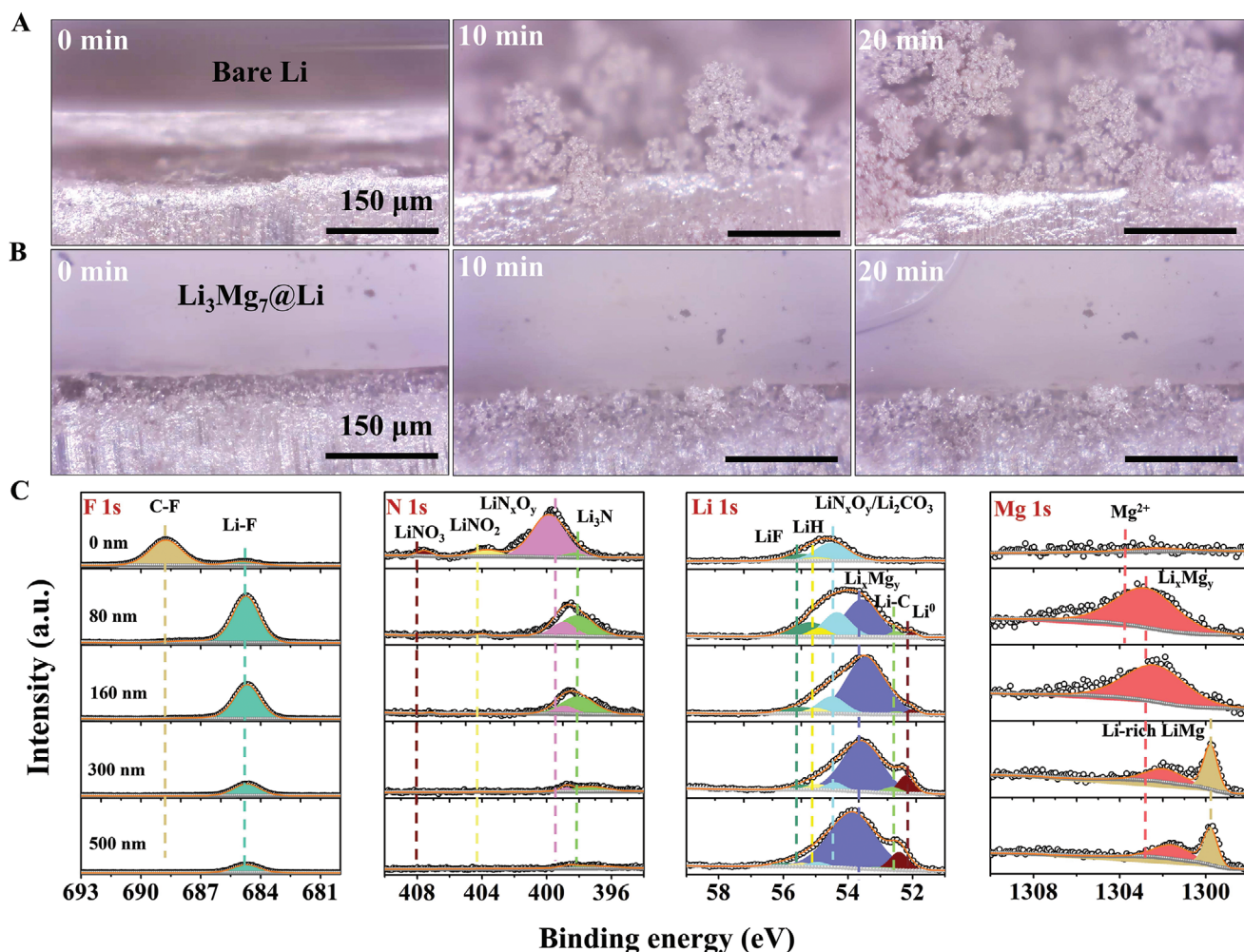


Figure 5. In situ optical observations of Li deposition on A) bare Li and B) $\text{Li}_3\text{Mg}_7@Li$ at 10 mA cm^{-2} after various times. C) XPS depth profile of $\text{Li}_3\text{Mg}_7@Li$ electrode after 20 cycles at 1 mA cm^{-2} for 1 mA h cm^{-2} .

spectroscopy (EDS) mapping and theoretical calculation results, facilitating the stabilization of LMAs.

The specific capacity of $\text{Li}_3\text{Mg}_7@Li$ with a thickness of 200 μm was first evaluated by galvanostatic charging method to confirm the ratio of Mg, LiH, and Li-containing polymers in the electrode. The voltage profile shows that a high specific capacity of 3408 mA h g^{-1} could be obtained, equaling to a weight ratio of 88.3 wt% for activated Li in $\text{Li}_3\text{Mg}_7@Li$ electrode, which is close to the theoretical specific capacity of Li (Figure S36, Supporting Information). In order to demonstrate the potential of $\text{Li}_3\text{Mg}_7@Li$ anode for practical application, full cells coupled with LFP cathode (denoted as $\text{Li}_3\text{Mg}_7@Li//LFP$) were first assembled and tested. Rate capability demonstrates that the cell of $\text{Li}_3\text{Mg}_7@Li//LFP$ presents higher reversible specific capacity of 160, 146, 135, 101, and 142 mA h g^{-1} at 0.2 C, 0.5 C, 1 C, 3 C, and 0.5 C, respectively, than that of Li//LFP full cell (Figure 6A). The improved capacity of $\text{Li}_3\text{Mg}_7@Li//LFP$ full cells could be attributed to the superior kinetics of $\text{Li}_3\text{Mg}_7@Li$ anode as verified by the lower overpotential in the discharge/charge profiles at various current densities (Figure 6B and Figure S37, Supporting Information).^[18,23] Long-term cycling

performance illustrates that the specific capacity of Li//LFP full cell shows rapid decay with a capacity retention of only 57.9% after 270 cycles owing to the formation of “dead Li” induced by repeated growth and isolation of Li dendrites (Figure S38A,B, Supporting Information). In sharp contrast, $\text{Li}_3\text{Mg}_7@Li//LFP$ full cell retains a high reversible capacity of 104 mA h g^{-1} after cycling for over 700 cycles with a capacity retention as high as 78.5% (Figure 6C) and lower voltage hysteresis than Li//LFP full cells (Figure S39, Supporting Information). The excellent cycling stability could be supported by the smooth and dense surface morphology of $\text{Li}_3\text{Mg}_7@Li$ electrode (Figure S38C,D, Supporting Information). The dendritic structure of Li_3Mg_7 alloys on the surface of $\text{Li}_3\text{Mg}_7@Li$ electrode, however, becomes indistinct owing to the spontaneous diffusion of Mg downward into Li metal. To further investigate the potential application of $\text{Li}_3\text{Mg}_7@Li$ under practical conditions, the electrochemical performance of full cells with a high mass loading of LFP cathode (LFP: 30 mg cm^{-2}) and lean electrolyte (the electrolyte/LFP mass ratio was controlled to be 1 $\mu\text{L mg}^{-1}$) were further investigated. Upon cycling at 0.5 C (Figure S40, Supporting Information), Li//LFP full cells exhibit rapid capacity decay after only

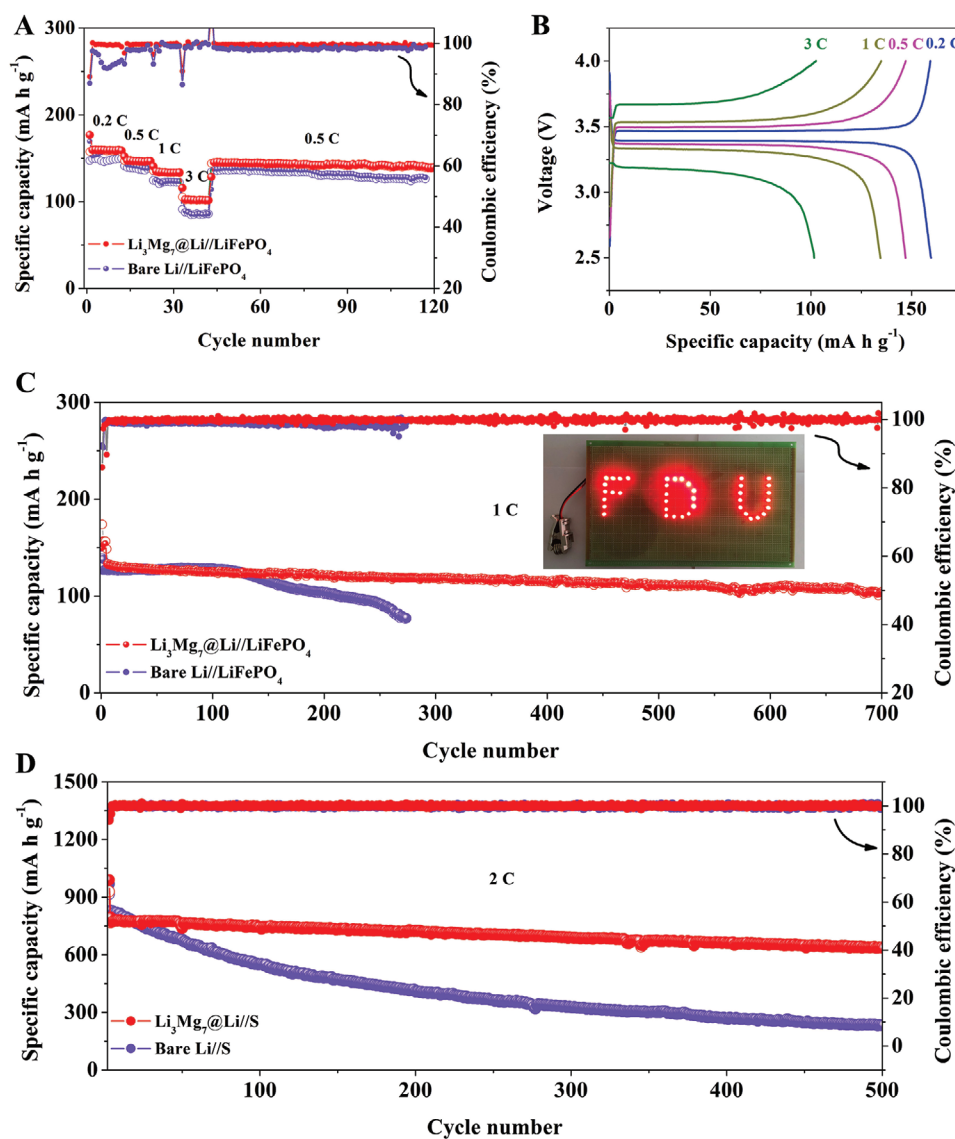


Figure 6. A) Rate performance of $\text{Li}_3\text{Mg}_7@/\text{Li}/\text{LFP}$ and bare Li/LFP full cells at various rates from 0.2 C to 3 C (1 C = 170 mA g⁻¹). B) Charge/discharge profiles of $\text{Li}_3\text{Mg}_7@/\text{Li}/\text{LFP}$ at various rates. C) Cycling performance of $\text{Li}_3\text{Mg}_7@/\text{Li}/\text{LFP}$ and bare Li/LFP full cells at 1 C. Inset is LEDs powered by $\text{Li}_3\text{Mg}_7@/\text{Li}/\text{LFP}$ full cells. D) Cycling performance of $\text{Li}_3\text{Mg}_7@/\text{Li}/\text{S}$ and bare Li/S at 2 C (1 C = 1670 mA g⁻¹).

47 cycles. In strong contrast, $\text{Li}_3\text{Mg}_7@/\text{Li}/\text{LFP}$ full cells present a stable cycling performance of over 100 cycles with an average capacity decay of only 0.05% per cycle and stable voltage profiles due to the favorable and uniform deposition/extraction of Li from $\text{Li}_3\text{Mg}_7@/\text{Li}$.

The advantages of $\text{Li}_3\text{Mg}_7@/\text{Li}$ electrode for practical application was subsequently evaluated in Li-S cells, which have been widely considered as one of the most promising next-generation rechargeable batteries.^[24] The $\text{Li}_3\text{Mg}_7@/\text{Li}/\text{S}$ full cell delivers a reversible capacity of 1036, 810, 700, and 485 mA h g⁻¹ at different rates of 0.5 C, 1 C, 2 C, and 4 C (1 C = 1670 mA g⁻¹), respectively (Figure S41, Supporting Information), much higher than that of Li/S full cells. The superior rate performance of $\text{Li}_3\text{Mg}_7@/\text{Li}/\text{S}$ full cells could be attributed to the lower polarization and better reaction kinetics than Li/S full cells based on the smaller potential difference between charge/discharge

plateaus of $\text{Li}_3\text{Mg}_7@/\text{Li}/\text{S}$ full cell (Figure S42, Supporting Information). Upon cycling at a high current density of 2 C (Figure 6D), Li/S full cell showed a rapid capacity fading with a capacity retention of only 28.2% after 500 cycles, while a reversible capacity of 640 mA h g⁻¹, corresponding to a capacity retention of 79.7%, could still be obtained for $\text{Li}_3\text{Mg}_7@/\text{Li}/\text{S}$ cell (Figure S43, Supporting Information). SEM images validate that, instead of fractured surface with the formation of “dead Li” layer observed for bare Li anode (Figure S44, Supporting Information), $\text{Li}_3\text{Mg}_7@/\text{Li}$ anode showed a dense and smooth surface morphology (Figure S45, Supporting Information) after 100 cycles. In addition, EDS mapping results demonstrated a massive accumulation of S species on the cracks of cycled bare Li anode (Figure S46, Supporting Information), which agrees well with the presence of strong peaks belonging to Li_2S_2 (161.5 eV)/ Li_2S (160.1 eV) in the XPS results of bare Li-metal

anode (Figure S47, Supporting Information). This result directly demonstrates the significant corrosion of bare Li by the shuttling polysulfide intermediates, which is also responsible for the rapid degradation of cycling performance. By contrast, uniform distribution of S species with a lower content could be obviously observed for the cycled $\text{Li}_3\text{Mg}_7/\text{Li}$ anode (Figure S48, Supporting Information) owing to the formation of MgS/MgO (1303.7 eV) during cycling, which could protect Li from corrosion by polysulfide intermediate (Figure S49, Supporting Information). It verifies that the presence of dendritic Li_3Mg_7 enriched with LiH and Li-containing polymers could not only guide the uniform and dense deposition of Li to ensure the well-preserved structural integrity of dendrite-free anode, but also alleviate the side reaction between Li and polysulfide intermediate, leading to the significantly enhanced cycling stability of $\text{Li}_3\text{Mg}_7/\text{Li}/\text{S}$ full cells.

3. Conclusion

In summary, we report the stabilization of LMAs by in situ building dendritic lithiophilic Li_3Mg_7 alloys enriched with LiH and Li-containing Li-polymers. The dendritic structure constructed by Li_3Mg_7 alloys could not only reduce the local current density, but also afford void space to accommodate the large volume change during cycling. More importantly, Li_3Mg_7 alloys could not only guide the uniform Li deposition down into the below Li metal upon Li plating, but also thermodynamically promote the extraction of Li from the thus-formed LiMg alloys during the reverse Li stripping process, which prevents the parasitic reactions between Li metal and electrolyte and hence leads to the formation of stable electrode/electrolyte interface. Furthermore, the thermodynamically favorable diffusion of Mg from Li_3Mg_7 alloys toward Li metal results in uniform distribution of LiMg alloys inside the whole electrode, resulting in long-term deep cycling stability. Consequently, the protected Li-metal anode exhibits excellent cycling stability both in symmetrical cells and in full cells. This proof-of-concept strategy in the rational design of 3D conductive structure on the surface of Li metal opens up a new avenue for stabilizing LMAs, which could also be further extended to the protection of Na or K metal anodes.

Supporting Information

Supporting Information is available from the Wiley Online Library or from the author.

Acknowledgements

This work was partially supported by the National Key R&D Program of China (no. 2018YFB1502101), National Science Fund for Distinguished Young Scholars (51625102), the National Natural Science Foundation of China (51971065, 51901045), the Innovation Program of Shanghai Municipal Education Commission (2019-01-07-00-07-E00028), the Science and Technology Commission of Shanghai Municipality (17XD1400700), and the Programs for Professor of Special Appointment (Eastern Scholar) at Shanghai Institutions of Higher Learning.

Conflict of Interest

The authors declare no conflict of interest.

Data Availability Statement

Data available on request from the authors.

Keywords

dendritic structures, Li-ion batteries, Li-metal anode, Li_3Mg_7

Received: November 13, 2020

Revised: January 22, 2021

Published online:

- [1] a) M. Armand, J. M. Tarascon, *Nature* **2008**, *451*, 652; b) J. W. Choi, D. Aurbach, *Nat. Rev. Mater.* **2016**, *1*, 16013.
- [2] a) X.-B. Cheng, R. Zhang, C.-Z. Zhao, Q. Zhang, *Chem. Rev.* **2017**, *117*, 10403; b) B. Liu, J.-G. Zhang, W. Xu, *Joule* **2018**, *2*, 833.
- [3] D. Lin, Y. Liu, Y. Cui, *Nat. Nanotechnol.* **2017**, *12*, 194.
- [4] Y. S. Cohen, Y. Cohen, D. Aurbach, *J. Phys. Chem. B* **2000**, *104*, 12282.
- [5] K. Yan, J. Wang, S. Zhao, D. Zhou, B. Sun, Y. Cui, G. Wang, *Angew. Chem., Int. Ed.* **2019**, *131*, 11486.
- [6] L. Liu, Y.-X. Yin, J.-Y. Li, S.-H. Wang, Y.-G. Guo, L.-J. Wan, *Adv. Mater.* **2018**, *30*, 1706216.
- [7] L. Suo, Y.-S. Hu, H. Li, M. Armand, L. Chen, *Nat. Commun.* **2013**, *4*, 1481.
- [8] Y. Li, Y. Li, A. Pei, K. Yan, Y. Sun, C.-L. Wu, L.-M. Joubert, R. Chin, A. L. Koh, Y. Yu, J. Perrino, B. Butz, S. Chu, Y. Cui, *Science* **2017**, *358*, 506.
- [9] I. T. Røe, S. M. Selbach, S. K. Schnell, *J. Phys. Chem. Lett.* **2020**, *11*, 2891.
- [10] a) H. Liu, X.-B. Cheng, J.-Q. Huang, S. Kaskel, S. Chou, H. S. Park, Q. Zhang, *ACS Mater. Lett.* **2019**, *1*, 217. b) Z. Hou, J. Zhang, W. Wang, Q. Chen, B. Li, C. Li, *J. Energy Chem.* **2020**, *45*, 7.
- [11] F. Guo, C. Wu, H. Chen, F. Zhong, X. Ai, H. Yang, J. Qian, *Energy Storage Mater.* **2020**, *24*, 635.
- [12] a) L. Wu, G. He, Y. Ding, *J. Mater. Chem. A* **2019**, *7*, 25415; b) L. Wang, S. Fu, T. Zhao, J. Qian, N. Chen, L. Li, F. Wu, R. Chen, *J. Mater. Chem. A* **2020**, *8*, 1247.
- [13] S. Xia, X. Zhang, C. Liang, Y. Yu, W. Liu, *Energy Storage Mater.* **2020**, *24*, 329.
- [14] Q. Xu, J. Lin, C. Ye, X. Jin, D. Ye, Y. Lu, G. Zhou, Y. Qiu, W. Li, *Adv. Energy Mater.* **2020**, *10*, 1903292.
- [15] a) H. Zhao, D. Lei, Y.-B. He, Y. Yuan, Q. Yun, B. Ni, W. Lv, B. Li, Q.-H. Yang, F. Kang, J. Lu, *Adv. Energy Mater.* **2018**, *8*, 1800266; b) S.-S. Chi, Q. Wang, B. Han, C. Luo, Y. Jiang, J. Wang, C. Wang, Y. Yu, Y. Deng, *Nano Lett.* **2020**, *20*, 2724; c) D. Zhang, A. Dai, M. Wu, K. Shen, T. Xiao, G. Hou, J. Lu, Y. Tang, *ACS Energy Lett.* **2020**, *5*, 180; d) Z. Luo, C. Liu, Y. Tian, Y. Zhang, Y. Jiang, J. Hu, H. Hou, G. Zou, X. Ji, *Energy Storage Mater.* **2020**, *27*, 124.
- [16] a) S.-S. Chi, Y. Liu, W.-L. Song, L.-Z. Fan, Q. Zhang, *Adv. Funct. Mater.* **2017**, *27*, 1700348; b) J. Zhu, J. Chen, Y. Luo, S. Sun, L. Qin, H. Xu, P. Zhang, W. Zhang, W. Tian, Z. Sun, *Energy Storage Mater.* **2019**, *23*, 539; c) C. Sun, Y. Li, J. Jin, J. Yang, Z. Wen, *J. Mater. Chem. A* **2019**, *7*, 7752.
- [17] a) C. Jin, O. Sheng, J. Luo, H. Yuan, C. Fang, W. Zhang, H. Huang, Y. Gan, Y. Xia, C. Liang, J. Zhang, X. Tao, *Nano Energy* **2017**, *37*,

- 177; b) K. Yan, Z. Lu, H.-W. Lee, F. Xiong, P.-C. Hsu, Y. Li, J. Zhao, S. Chu, Y. Cui, *Nat. Energy* **2016**, *1*, 16010; c) H. Wang, Y. Li, Y. Li, Y. Liu, D. Lin, C. Zhu, G. Chen, A. Yang, K. Yan, H. Chen, Y. Zhu, J. Li, J. Xie, J. Xu, Z. Zhang, R. Vila, A. Pei, K. Wang, Y. Cui, *Nano Lett.* **2019**, *19*, 1326.
- [18] R. Zhang, X. Chen, X. Shen, X.-Q. Zhang, X.-R. Chen, X.-B. Cheng, C. Yan, C.-Z. Zhao, Q. Zhang, *Joule* **2018**, *2*, 764.
- [19] a) Y. Wang, J. Lv, L. Zhu, Y. Ma, *Comput. Phys. Commun.* **2012**, *183*, 2063; b) Y. Wang, J. Lv, L. Zhu, Y. Ma, *Phys. Rev. B* **2010**, *82*, 094116.
- [20] a) M. S. Kim, S. H. L. Deepika, M.-S. Kim, J.-H. Ryu, K.-R. Lee, L. A. Archer, W. I. Cho, *Sci. Adv.* **2019**, *5*, eaax5587; b) M. Li, B. Sun, Z. Ao, T. An, G. Wang, *J. Mater. Chem. A* **2020**, *8*, 10199.
- [21] A. Pei, G. Zheng, F. Shi, Y. Li, Y. Cui, *Nano Lett.* **2017**, *17*, 1132.
- [22] a) Y. Liu, D. Lin, Z. Liang, J. Zhao, K. Yan, Y. Cui, *Nat. Commun.* **2016**, *7*, 10992; b) J. Heine, S. Krüger, C. Hartnig, U. Wietelmann, M. Winter, P. Bieker, *Adv. Energy Mater.* **2014**, *4*, 1300815.
- [23] L. Liu, Y.-X. Yin, J.-Y. Li, N.-W. Li, X.-X. Zeng, H. Ye, Y.-G. Guo, L.-J. Wan, *Joule* **2017**, *1*, 563.
- [24] a) T. Liu, H. Hu, X. Ding, H. Yuan, C. Jin, J. Nai, Y. Liu, Y. Wang, Y. Wan, X. Tao, *Energy Storage Mater.* **2020**, *30*, 346; b) X. Ji, K. T. Lee, L. F. Nazar, *Nat. Mater.* **2009**, *8*, 500; c) W. Li, H. Yao, K. Yan, G. Zheng, Z. Liang, Y.-M. Chiang, Y. Cui, *Nat. Commun.* **2015**, *6*, 7436.